Proceedings of Engineering and Technology Innovation, vol. 33, 2026, pp. 132-147

Self-Recovering Crosslinked Natural Rubber Sensors for Vascular Simulation in Wireless Electro-Syringe Injection

Korn Taksapattanakul[1,*], Panisara Wanmahamart[2]

[1]Faculty of Science and Technology, Princess of Naradhiwas University, Narathiwat Province, Thailand

[2]Faculty of Science and Technology, PNU Wittayanusorn School, Princess of Naradhiwas University, Narathiwat Province, Thailand

Received 19 March 2026; revised 20 April 2026; accepted 21 April 2026

DOI: https://doi.org/10.46604/peti.2026.16290

Abstract

Safe injection technique is recognized as a critical competency in medical training, yet access to realistic and affordable simulators remains limited. This study aims to develop a wireless electro-syringe system that incorporates a self-recovering crosslinked natural rubber sensor for vascular tissue response. The sensor is fabricated from natural rubber latex via controlled sulfur vulcanization, enabling autonomous structural recovery after repeated needle penetrations. A closed-circuit detection system delivers immediate feedback upon overpenetration, providing real-time performance guidance. Fourier transform infrared spectroscopy (FTIR) analysis confirms a reduction of carbon-carbon double bonds and the formation of carbon-sulfur crosslinks. Increasing vulcanization temperature and curing time enhances crosslinking density and improves mechanical performance and self-recovery properties. Diffusion analysis confirms Fickian behavior ($n \approx 0.5$) with an activation energy of 31.244 $kJ \cdot mol^{-1}$. The elastic modulus gradually recovers after disruption, suggesting effective network reformation. Overall, this work provides a low-cost, reusable, and mechanically realistic solution for injection training.

Keywords: natural rubber vulcanization, self-recovering crosslinked network, vascular simulation sensor, injection training device, Fick's second law

1. Introduction

Injection techniques are among the most common clinical procedures, requiring both procedural skills and knowledge of injection site anatomy. However, instructional approaches for teaching these skills remain insufficiently studied. Recently, educators have adopted more realistic and engaging training tools to complement traditional methods and enhance learning across cognitive, affective, and psychomotor domains.

Innovation in physical simulation has advanced considerably. Studies have demonstrated the development of cost-effective intramuscular injection simulators that replicate key anatomical structures and tissue textures, improving both student confidence and practical competency [1]. Another study describes a multilayer needle injection pad trainer that simulates intradermal, subcutaneous, and intramuscular injections. Educators and students report that the device closely resembles the tactile properties of human tissue [2]. Additionally, using tomatoes as a preliminary injection training activity reduced student anxiety and improved needle handling skills before first patient contact [3].

Digital and immersive learning technologies have expanded training options. Studies show that virtual learning environments offer a scalable and engaging alternative to procedural training and can complement traditional methods to enhance clinical competence [4]. Virtual reality-based instruction improved engagement, knowledge retention, and emotional

*Corresponding author. E-mail address: korn.t@pnu.ac.th

involvement during ventrogluteal injection training, though limitations in the system design were noted [5]. A webXR module integrating virtual, augmented, and mixed reality technologies provides flexible clinical simulations across multiple devices and improves procedural understanding [6]. The ARSim2care augmented reality application, running on Microsoft HoloLens, was positively received by over 90% of nursing students, who reported improved motivation, theoretical retention, and anatomical understanding [7].

Pedagogical approaches have evolved alongside technological developments. Active learning strategies, such as combining the flipped classroom model with Kahoot-based game learning, significantly improved nursing students' knowledge, psychomotor performance, and self-efficacy during injection training [8]. Animated video training that incorporates subliminal procedural cues improved step recall, although it did not significantly affect anxiety or self-confidence [9]. Blended learning, which integrates workshops, e-learning, and hands-on practice, improved nurses' knowledge and practical skills in ventrogluteal injection training [10]. Computer-based simulation was particularly effective for cognitive and psychomotor outcomes. Hybrid methods, however, better address affective learning. These findings suggest that combining approaches may offer the most balanced strategy for clinical training [11].

Alongside educational innovation, prior research developed technologies to improve injection accuracy and procedural safety. Ultrasound-guided injection has enabled precise placement within muscle tissue [12], while other studies have emphasized the need for biologically relevant in vitro models [13] and demonstrated that robotic palpation with tactile sensing could reconstruct three-dimensional tissue structures [14]. However, a key limitation remained unresolved. High-fidelity physical simulators lack structural recovery after repeated needle penetration and therefore require frequent replacement, whereas digital platforms, although reusable, do not replicate the mechanical behavior of real vascular tissue. At the time of this study, only limited reports have described a low-cost, electronically instrumented injection trainer that integrates a self-recovering, biologically analogous material with real-time multimodal feedback across repeated training cycles.

The present study is undertaken to address this gap. To help users practice and improve their vascular injection skills, a wireless electro-syringe injection training device is developed using readily available, low-cost electronic components. Configured to deliver immediate visual and auditory alerts if the needle is inserted too deeply during simulated injections, the device provides real-time feedback for trainees. A self-recovering crosslinked natural rubber vascular simulation sensor, chosen for its mechanical similarity to real vascular tissue under needle penetration, is integrated into the system. Its ability to restore structural integrity after mechanical disruption allows for repeated, cost-effective training without component replacement. To validate material suitability, the sensor is characterized using crosslink density, Fickian diffusion, Fourier-transform infrared spectroscopy, and time-dependent mechanical recovery.

2. Materials and Methods

This section describes the design and fabrication of the proposed device, along with the preparation of the self-recovering natural rubber sensor. It also outlined the experimental procedures and characterization techniques used to evaluate material properties and system performance. The influence of curing conditions on the crosslinking structure and sensing performance was systematically investigated. The relationship between material structure and recovery behavior was also evaluated.

2.1. Materials

Components for the wireless electro-syringe injection, including Circuit Wizard software, switch, LED, buzzer, DC battery, cable wire clips, sensor sheet, and syringe with needle, were sourced from suppliers in Narathiwat, Thailand. The base material for fabricating the autonomously self-recovering crosslinked natural rubber vascular simulation sensor, as listed in Table 1, was procured from vendors in Bangkok, Thailand.

Table 1 Formulation of self-recovering crosslinked natural rubber vascular sensor

Materials	Concentration	Loading (phr)*
Natural rubber latex	40% DRC	100
Zinc oxide dispersion	50%	1.5-2.0 (± 0.5)
Sulfur dispersion	50%	1.0-1.5 (± 0.5)
ZMBT, zinc 2-Mercaptobenzo-thiazole dispersion	50%	1.0-1.5 (± 0.05)
ZDEC, zinc Diethyldithiocarbamate dispersion	50%	0.5-1.0 (± 0.05)

*phr = parts per hundred rubber

2.2. Circuit Design of the Wireless Electro-Syringe Injection

The wireless electro-syringe injection was developed based on fundamental electronics principles using Circuit Wizard software for design, simulation, and verification before physical construction, as shown in Fig. 1. The circuit operates through three functional states determined by the switch position and the connection status between sensing layers 1 and 3. When the switch is open, the circuit is interrupted, and both the LED and buzzer remain inactive (Fig. 1(a)). When the switch is closed while layers 1 and 3 remain unconnected, current flows through the main circuit; however, the LED and buzzer remain inactive (Fig. 1(b)-Fig. 1(c)). When the conductive needle penetrates sufficiently to bridge sensing layers 1 and 3, the circuit is fully completed (Fig. 1(d), allowing current to flow, activating the LED and buzzer simultaneously to deliver immediate visual and auditory feedback to the trainee.

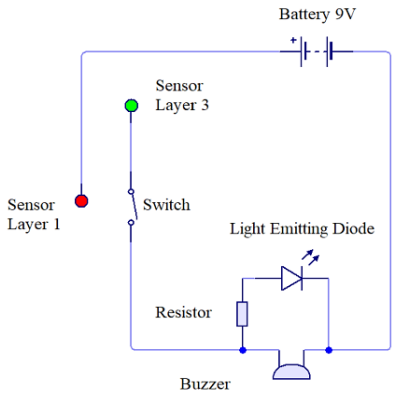

(a) Circuit interrupted, LED and buzzer inactive

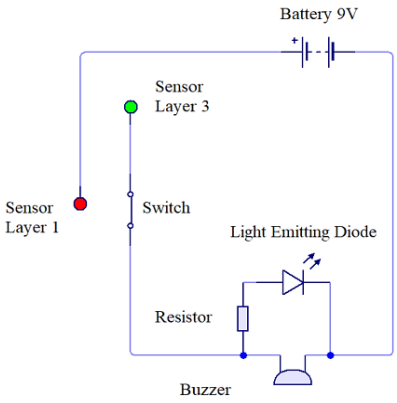

(b) Sensing unconnected, LED and buzzer inactive

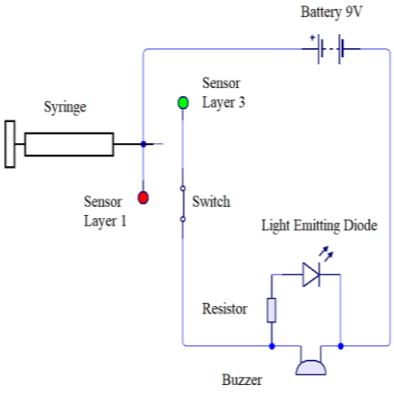

(c) Conductive needle in contact, LED and buzzer inactive

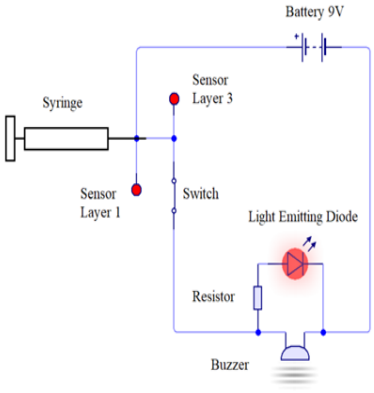

(d) Circuit fully completed, LED and buzzer active

Fig. 1 Circuit diagram of the wireless electro-syringe injection designed using Circuit Wizard software

After verification of the circuit design, the schematic was translated into a physical printed circuit board (PCB) layout. Electronic components, including an LED, a buzzer, resistors, a power supply, and a switch, were arranged and integrated according to the verified schematic (Fig. 2). The fully assembled PCB was then incorporated into the complete device to produce the wireless electro-syringe injection (Fig. 3).

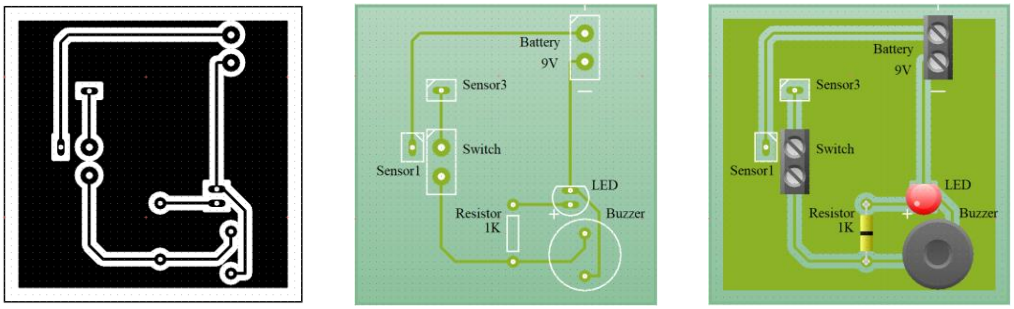

(a) Artwork PCB layout (b) Logic level diagram (c) Real printed

Fig. 2 Design of the printed circuit board (PCB) for the wireless electro-syringe injection system

(a) Internal circuit components (b) Complete unit (c) Circuit functionality test

Fig. 3 Photographs of the wireless electro-syringe injection

2.3. Fabrication of the Autonomously Self-Recovering Crosslinked Natural Rubber Vascular Simulation Sensor

A natural rubber compound was prepared with vulcanization chemicals at 25 ± 5°C and cast into a mold to create the vascular simulation sensor and sheet. Two curing methods were used to investigate the effect of curing conditions on the crosslinking and self-recovery behavior of the sensor: thermal vulcanization in a hot-air oven at 30, 40, and 50°C for 7 days, and pre-curing at 30°C for 7 days followed by room-temperature curing for 28 days. The final sensor had a hollow, sphere-like structure with a 2 mm wall thickness and a sensing element mounted on the vessel lumen surface, as shown in Fig. 4.

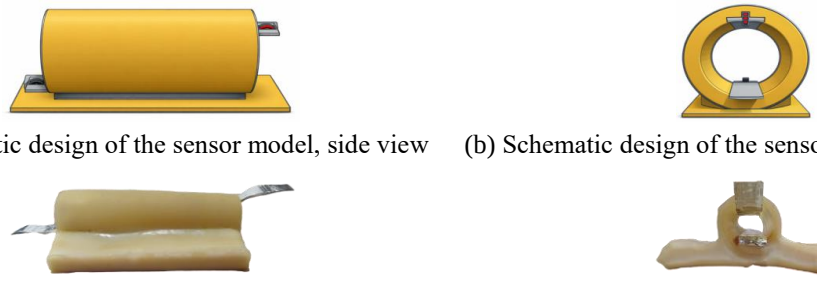

(a) Schematic design of the sensor model, side view (b) Schematic design of the sensor model, front view

(c) Fabricated sensor model, side view (d) Fabricated sensor model, front view

Fig. 4 Autonomously self-recovering crosslinked natural rubber vascular sensor

2.4. Controlled Crosslinking Analysis of the Autonomously Self-Recovering Natural Rubber Vascular Simulation Sensor

The crosslinking behavior of the natural rubber and the self-recovery vascular simulation sensor was investigated by varying vulcanization temperature and curing time. Crosslink density is closely related to the mechanical properties and self-recovery performance of the rubber sensor. This approach allows quantitative evaluation of polymer network crosslinking via swelling measurements. First, crosslink density was determined using the Flory-Rehner equation. Swelling behavior was evaluated using ASTM D3616-95 [15]. For these tests, specimens were cut and weighed to obtain dry masses of 0.39-0.41 g, and then immersed in 25 cm^3 of toluene (AR grade toluene typically has purity, 99.5%) in sealed containers stored in the dark at 25 ± 2°C for 24 h. After immersion, specimens were removed from the toluene, blotted with tissue paper to remove surface solvent, and then reweighed. The sample was performed in triplicate, and the results were recorded.

2.4.1. Determination of Crosslink Density

The crosslink density was determined using the Flory-Rehner equation [16-18]. The equation is expressed below:

$$\eta_{swell} = \frac{-\ln(1-V_r) - V_r - \chi V_r^2}{2V_s \times (V_r^{1/3} - \frac{2V_r}{f})} \tag{1}$$

where η_{swell} is cross-link density of the rubber (mol/cm^3) via swelling behavior, V_r is volume fraction of rubber in swollen gel, χ is rubber-toluene solvent interaction parameter (0.3795), V_s is molar volume of the toluene (106.2 cm^3/mol), and f is functionality of the crosslinks (being 4 for sulfur vulcanizing system).

$$V_r = \frac{\frac{(W_d - W_f)}{\rho_r}}{\frac{(W_d - W_f)}{\rho_r} + \frac{(W_s - W_d)}{\rho_s}} \tag{2}$$

where V_r is volume fraction of rubber in swollen gel, W_d is the weight (g) of the de-swollen sample, W_f is the weight (g) of the filler in the compound, W_s is the weight (g) of the swollen sample, and ρ_s is the density of the toluene solvent (0.87 g/cm^3), and ρ_r is the density of the rubber (0.91 g/cm^3).

2.4.2. Swelling Behavior Analysis

The swelling percentage at time (Q_t) was calculated using the equation below in line with ASTM D3616-95 [15, 17]:

$$Q_t = \frac{\frac{(W_t - W_o)}{W_o}}{M_W} \cdot 100 \tag{3}$$

where W_o is the weight of dry sample (g), W_t is the weight of swollen sample (g), and M_W is the molar mass of toluene (92.14 g /mol).

2.4.3. Solvent Diffusion Analysis using Fick's Second Law

Solvent diffusion analysis was performed using natural rubber sheets cured at 30°C for 7 days, in accordance with ASTM D471 [19]. Specimens of 2 mm thickness and initial dry mass (g) (W_o) of 0.10 g were immersed in toluene at controlled temperatures of 25, 30, 35, 40, 45, and 50°C using a hotplate, and mass (g) uptake (W_t) was recorded at 5 min intervals from 5 to 60 min until equilibrium was reached. The diffusion coefficient (D) can be calculated as:

$$D = \left(\frac{slope}{\frac{4}{h\sqrt{\pi}}}\right)^2 \tag{4}$$

where h is thickness in meters, D is diffusion coefficient, π is a constant value (3.14), and slope is the $\frac{M_t}{M_\infty}$ versus $\sqrt{t}$ plot at the initial linear region, according to the following expression [20-21]:

$$\frac{M_t}{M_\infty} = k\sqrt{t} \tag{5}$$

where M_t is mass (g) uptake at time (M_t=W_t-W_o), M_∞ is mass (g) uptake at equilibrium (M_∞= W_∞–W_o), k is swelling rate constant, t is time (min)

The empirical power-law expression was used to further characterize the transport mechanism. The Korsmeyer-Peppas model was applied to determine the diffusion exponent (n) [22]. This model provides insight into the solvent transport behavior and diffusion mechanism within the crosslinked rubber network. For experimental kinetic analysis:

$$\frac{M_t}{M_\infty} = kt^n \tag{6}$$

where M_t is mass (g) uptake at time (M_t=W_t– W_o), M_∞ is mass (g) uptake at equilibrium (M_∞=W_∞–W_o), k is swelling rate constant, t is time (min), n is the diffusion exponent for Fickian kinetics.

$$\ln(\frac{M_t}{M_\infty}) = \ln k + n\ln t \tag{7}$$

where n = 0.5 is Fickian diffusion, $0.5\langle n\langle 1$ is non-Fickian, n =1 is case II transport.

The temperature dependence of the diffusion coefficient (D) was evaluated using the Arrhenius relationship, from which the activation energy of diffusion (E_a) was determined according to the following expression [20-21]:

$$D = D_o \cdot \mathrm{e}^{-\frac{E_a}{RT}} \tag{8}$$

Taking the natural logarithm of Eq. (8):

$$\ln D = \ln D_o - \frac{E_a}{R}\frac{1}{T} \tag{9}$$

where D_0 is pre-exponential factor (diffusion constant), E_a is activation energy (J/mol), R is gas constant (8.314 J·mol^{-1}·K^{-1}), T is absolute temperature (K).

The activation energy of diffusion (E_a), was determined from the slope of the ln D versus $\frac{1}{T}$ plot. For sulfur-cured natural rubber, a low value in the range of 20-35 kJ·mol^{-1} indicates a flexible network with relatively low crosslink density and minimal resistance to solvent penetration. In contrast, a higher value in the range of 40-70 kJ·mol^{-1} reflects a more tightly crosslinked and structurally rigid network, in which greater chain resistance results in slower diffusion [21, 23].

2.5. Fourier Transform Infrared Spectroscopy (FTIR) Analysis

Rubber specimens were sectioned into 1 cm × 1 cm pieces and analyzed using an FTIR spectrometer in attenuated total reflectance (ATR) mode using a diamond crystal over the wavenumber range of 500-4000 cm^{-1} with a resolution of 2 cm^{-1}. Spectra were processed using OPUS software, and peak positions and integrated areas were determined using OriginPro. FTIR analysis was used to monitor the chemical changes associated with the vulcanization and crosslinking reactions in the rubber network. The conversion (%) was quantified from the reduction in the C=C stretching absorption band and the corresponding increase in the C-S stretching band, both normalized against a stable reference band [24-25], as expressed below:

$$\%conversion = (1 - \frac{(\frac{A_{C=C}}{A_{ref}})_{Vulcanized}}{(\frac{A_{C=C}}{A_{ref}})_{initial}}) \cdot 100 \tag{10}$$

$$\%conversion = (\frac{(\frac{A_{C-S}}{A_{ref}})_{Vulcanized}}{(\frac{A_{C-S}}{A_{ref}})_{initial}} - 1) \cdot 100 \tag{11}$$

where $A_{C=C}$ = absorbance or integrated area of the C=C stretching band (1600-1665 cm^{-1})

$A_{C\text{-}S}$ = absorbance or integrated area of the C-S stretching band (640-735 cm^{-1})

A_{ref} = absorbance of a reference band (CH_3 bending at 1328-1380cm^{-1}).

2.6. Tensile Characterization of the Autonomously Self-Recovering Crosslinked Natural Rubber

This section presents the tensile characterization of the autonomously self-recovering crosslinked natural rubber. The tests were conducted to evaluate mechanical strength, elasticity, and recovery behavior after deformation.

2.6.1. Stress–Strain Behavior

Tensile testing was conducted using a tensile testing machine (model H 10KS, Hounsfield Test Equipment, UK) at a crosshead speed of 50 ± 5 mm·min^{-1} in accordance with ASTM D412 [26]. The specimens, with a thickness of 3 ± 0.5 mm, were cured at 30°C for 7 days. Each specimen was cut into two equal pieces and then rejoined at 30°C and allowed to recover autonomously for 60, 120, and 180 min before testing. Subsequently, the specimens were subjected to uniaxial tensile loading until failure. The tensile strength at break was recorded and calculated as:

$$TS = \sigma = \frac{F}{A} \tag{12}$$

where TS is tensile strength at break (N/m^2 or Pa), σ is uniaxial stress (N/m^2 or Pa), F is the applied load (N), and A is the original cross-sectional area (m^2).

2.6.2. Young's Modulus in the Linear Elastic Region

At low strain, Young's modulus was determined from the slope of the stress-strain curve within the linear elastic region using the equation below [27]:

$$E = \frac{\sigma}{\varepsilon} = slope = \frac{\Delta\sigma}{\Delta\varepsilon} \tag{13}$$

where E is Young's modulus or modulus of elasticity (Pa), σ is stress (Pa), ε is strain.

2.6.3. Estimation of Crosslink Density from Rubber Elasticity Theory

Crosslink density was estimated from tensile test data using Young's modulus, derived from the slope of the initial linear region of the stress-strain curve, since, according to classical rubber elasticity theory [28], it is given by:

$$E = 3G \tag{14}$$

where G is shear modulus (Pa), E is Young's modulus (Pa).

According to classical rubber elasticity theory:

$$G = \upsilon RT \tag{15}$$

where υ is crosslink density (mol·m^{-3}), R is gas constant (8.314 J·mol^{-1}·K^{-1}), T is absolute temperature (K).

Substituting Eq. (14) into Eq. (15), the following expression is obtained:

$$\upsilon = \frac{E}{3RT} \tag{16}$$

where E is Young's modulus (Pa), T is absolute temperature (K), R is gas constant (8.314 J·mol^{-1}·K^{-1}), υ is crosslink density (mol·m^{-3}). This is the most commonly used equation to calculate crosslink density from Young's modulus.

2.7. Surface Morphological of the Autonomously Self-Recovering Crosslinked Natural Rubber Vascular Model

The surface morphology was examined using optical microscopy at 10× magnification, and photographs were processed in ImageJ [16] to visualize surface-localized deformation features associated with the self-recovery process. The same surface region of each specimen was imaged before and after tensile loading, and differences in defect morphology were used to assess the crosslinked rubber network's ability to restore surface integrity autonomously following mechanical deformation.

2.8. Design and Functional Analysis of the Wireless Electro-Syringe Injection

During assembly, the buzzer, LED, and switch were mounted on the outer surface of a plastic enclosure, while the PCB and battery were secured inside the casing. Alligator clip cable fasteners were used to connect to the dual-layer aluminum foil sensing elements embedded within the vascular simulation model, as shown in Fig. 5.

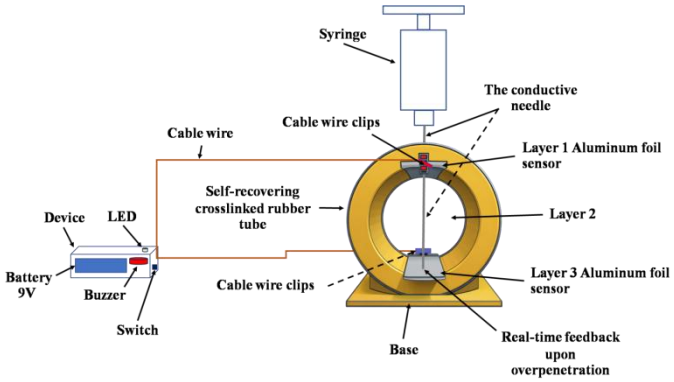

Fig. 5 Operational mechanism of the wireless electro-syringe injection system with a self-recovering rubber vascular model

3. Results and Discussion

This section presents and discusses the performance of a self-recovering crosslinked natural rubber sensor developed for wireless electro-syringe injection training. Emphasis is placed on vulcanization-induced network formation, mechanical recovery, and real-time feedback behavior of the closed-circuit detection system.

3.1. Effect of Vulcanization Conditions on Natural Rubber Network Structure

Figs. 6(a) and 6(b) show the FTIR spectra of natural rubber samples vulcanized at 30, 40, and 50°C with curing times of 7, 14, 21, and 28 days, recorded over a wavenumber range of 600-3900 cm^{-1}. A prominent band observed at 1600-1665 cm^{-1} region corresponds to C=C stretching vibrations of the polyisoprene backbone [25, 29]. A slight reduction in peak intensity with increasing temperature and time indicates progressive consumption of unsaturated double bonds during crosslink formation [29]. The band in the 1328-1380 cm^{-1} region, attributed to C-H bending vibrations of methyl and methylene groups [25, 29], remains stable across all spectra. This stability confirms that the hydrocarbon framework was unaffected by vulcanization. In contrast, the absorption band in the 640-735 cm^{-1} region, associated with C-S stretching vibrations [25, 29], increases in intensity with higher curing temperature and longer curing time. This increase confirms that enhanced sulfur crosslink formation occurs at higher temperatures and longer times [29], consistent with greater crosslink density and reduced swelling behavior.

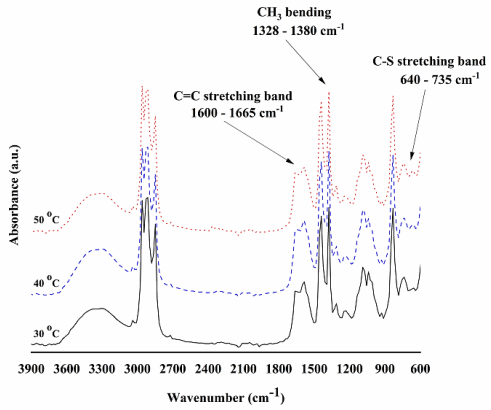

(a) FTIR spectra of natural rubber vulcanized at 30, 40, and 50°C for 7 days

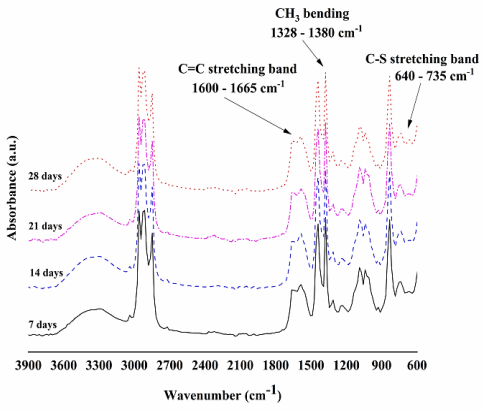

(b) FTIR spectra of natural rubber vulcanized at 30°C for 7, 14, 21, and 28 days

Fig. 6 FTIR spectra of vulcanized natural rubber under different vulcanization conditions

Fig. 7(a) presents the FTIR peak area ratios of C=C/CH_3 and C-S/CH_3 as a function of vulcanization temperature (30-50°C), derived from Fig. 6(a). The C=C/CH_3 ratio decreases with increasing temperature, while the C-S/CH_3 ratio increases, indicating temperature-dependent formation of C-S bonds associated with crosslinking [30]. Fig. 7(b) shows that the reaction conversion (%) of both C=C and C-S bands increased with temperature, with slightly higher C=C conversion at elevated temperatures.

Fig. 7(c) illustrates the variation of C=C/CH_3 and C-S/CH_3 ratios with vulcanization time at 30°C, based on Fig. 6(b). A continuous decrease in C=C/CH_3 and an increase in C-S/CH_3 were observed, confirming progressive crosslink formation during extended ambient curing. Fig. 7(d) demonstrates that the reaction conversion (%) of C=C and C-S bands increased with time, reflecting contributions from polysulfidic crosslink formation and intramolecular reactions that consume double bonds, although not all contribute directly to network formation [30].

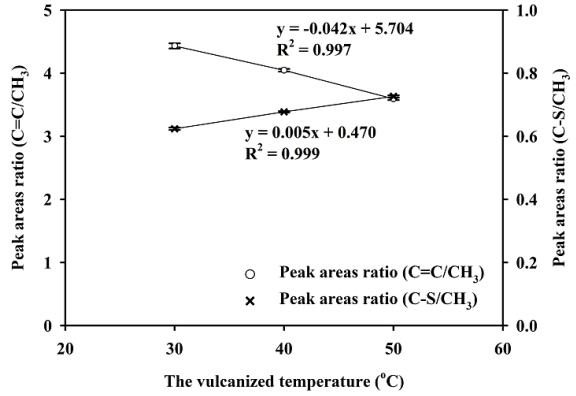

(a) Peak area ratios versus the vulcanization temperature

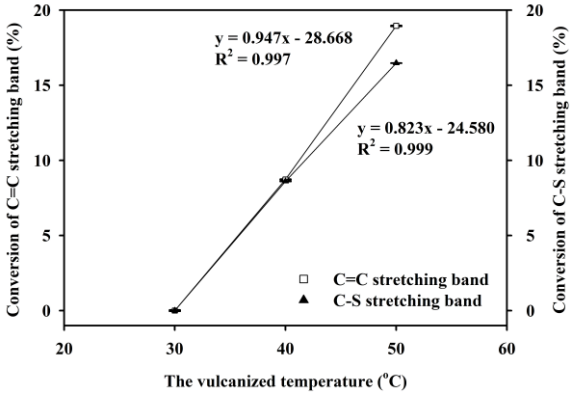

(b) Conversion (%) versus the vulcanization temperature

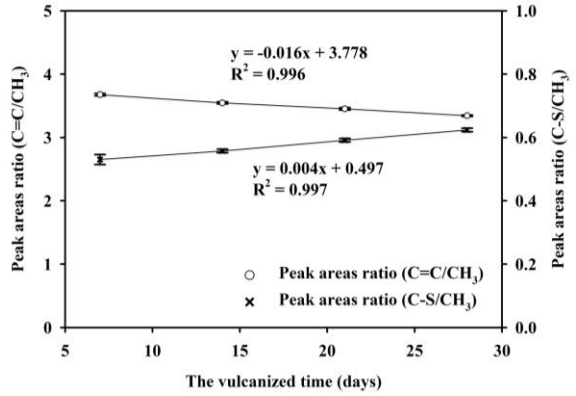

(c) Peak area ratios versus the vulcanization time at 30°C

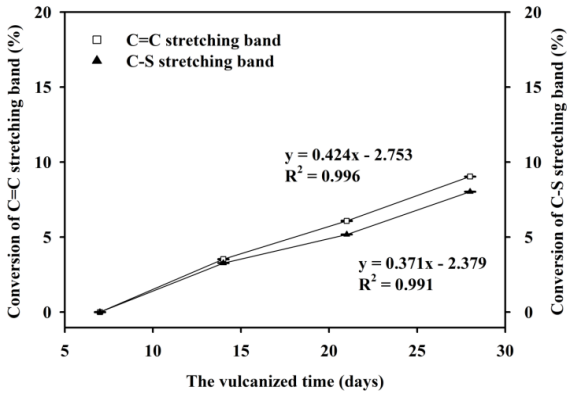

(d) Conversion (%) versus the vulcanization time at 30°C

Fig. 7 Effect of vulcanization conditions on the FTIR peak area ratios and reaction conversion of sulfur-vulcanized natural rubber

Fig. 8(a) shows the relationship between swelling percentage and crosslink density of vulcanized natural rubber as a function of vulcanization temperature (30-50°C) and vulcanization time (7-28 days). The decrease in swelling percentage with increasing crosslink density demonstrates that higher vulcanization temperature and longer curing time directly result in a more densely crosslinked and solvent-resistant network structure [28].

In Fig. 8(b), the decrease in swelling percentage and increase in crosslink density over recovery periods of 60, 120, and 180 min indicate that the crosslinked network continues to evolve during autonomous self-recovery under ambient conditions, driven by ongoing network reconstruction. Extended recovery time enables further network reconstruction, producing a more structurally developed elastomeric network [28], consistent with the time-dependent mechanical recovery.

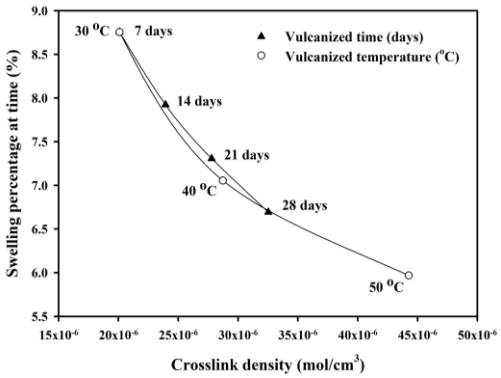

(a) Swelling percentage versus crosslink density of vulcanization temperature and time

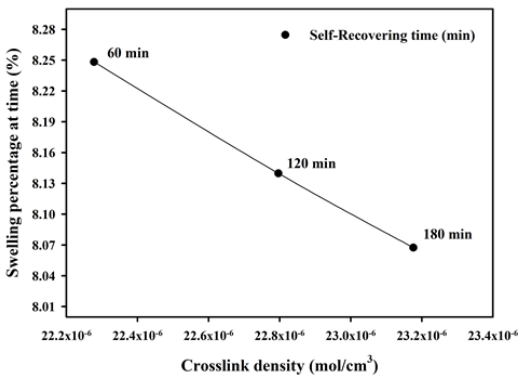

(b) Swelling percentage versus crosslink density of self-recovering time

Fig. 8 Relationship between swelling percentage and crosslink density of sulfur-vulcanized natural rubber under different vulcanization and self-recovery conditions

3.2. Self-Recovery Behavior and Structural Evolution of Vulcanized Natural Rubber

Fig. 9(a) shows the FTIR spectra of the rubber samples at self-recovery times of 0, 60, 120, and 180 min over 600-3900 cm-1. As recovery time increases, the intensity of the C=C stretching band at 1600-1665 cm-1[25, 29] decreases, while the C-S stretching band at 640-735 cm-1[25, 29] increases, and the C-H bending band at 1328-1380 cm-1[25, 29] remains stable. Fig. 9(b) presents the time-dependent FTIR peak area ratios of C=C/CH3 and C-S/CH3, showing decreases in C=C/CH3 and increases in C-S/CH3. Fig. 9(c) further presents the reaction conversion (%) of the C=C and C-S stretching bands over recovery time, illustrating a steady increase in C-S band conversion. This progression indicates a progressive construction of the crosslinked rubber network at the rejoined interface and confirms that the self-recovery mechanism involves the same sulfur crosslinking chemistry as original vulcanization [24].

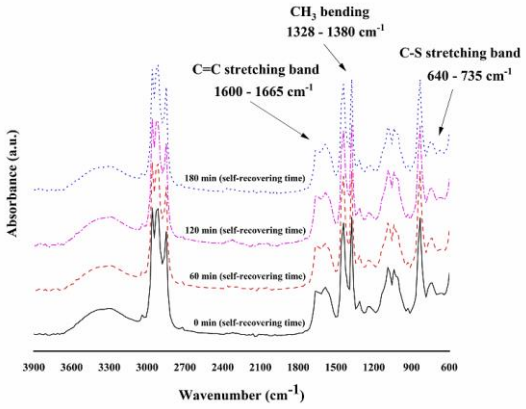

(a) FTIR spectra of the crosslinked natural rubber during the self-recovery process at 0, 60, 120, and 180 min

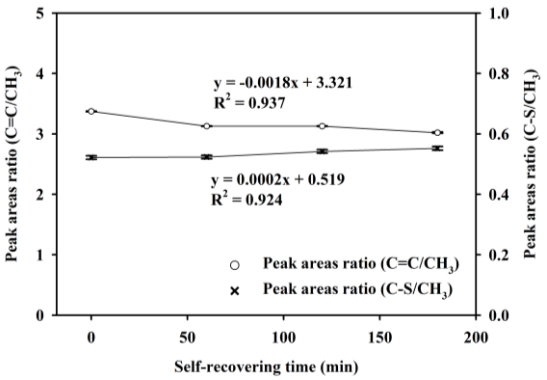

(b) Peak area ratios versus self-recovering time

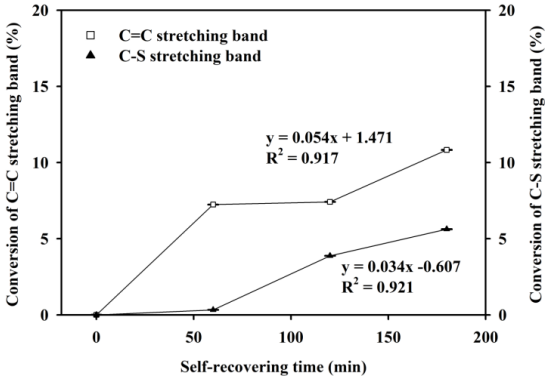

(c) Conversion (%) versus self-recovering time

Fig. 9 FTIR spectra and quantitative analysis of crosslinked natural rubber during the self-recovery process

Vulcanization at 30°C for 7 days produced a self-recovering natural rubber structure. Crosslinking under these mild conditions was evaluated using diffusion analysis based on Fick's second law. The activation energy (E_a) for diffusion was also determined. These results suggest that effective crosslinking occurs at low temperature within 7 days, forming the structural basis for the network's autonomous self-recovery behavior. To further understand the temperature-dependent diffusion behavior of the crosslinked network, a systematic swelling analysis was conducted.

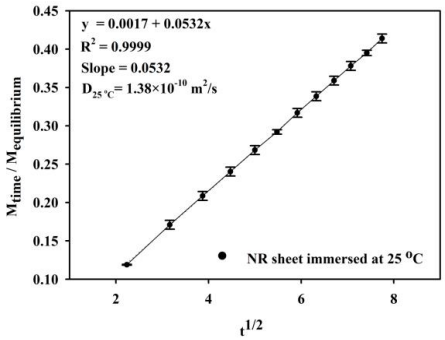

(a) $M_{time}/M_{equilibrium}$ and $t^{1/2}$ of NR sheets immersed in toluene at 25°C

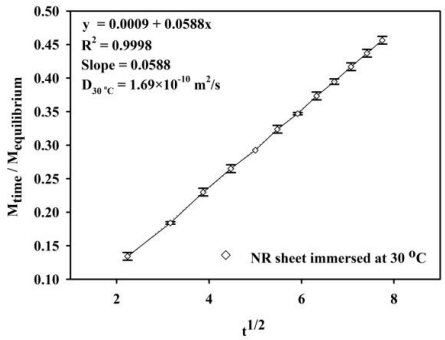

(b) $M_{time}/M_{equilibrium}$ and $t^{1/2}$ of NR sheets immersed in toluene at 30°C

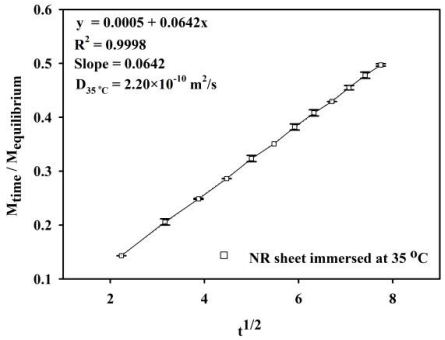

(c) $M_{time}/M_{equilibrium}$ and $t^{1/2}$ of NR sheets immersed in toluene at 35°C

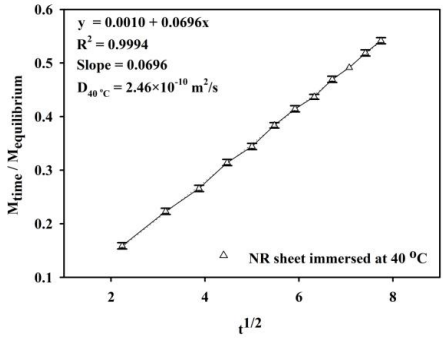

(d) $M_{time}/M_{equilibrium}$ and $t^{1/2}$ of NR sheets immersed in toluene at 40°C

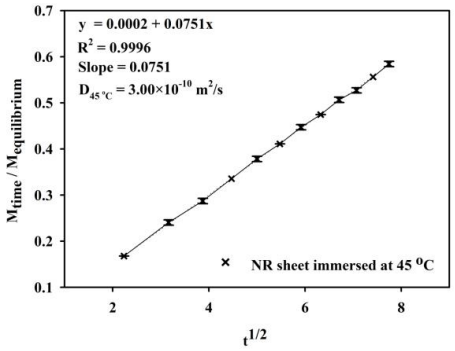

(e) $M_{time}/M_{equilibrium}$ and $t^{1/2}$ of NR sheets immersed in toluene at 45°C

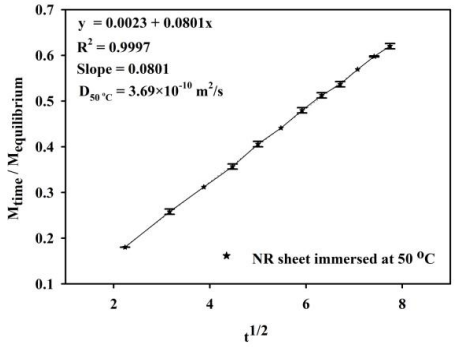

(f) $M_{time}/M_{equilibrium}$ and $t^{1/2}$ of NR sheets immersed in toluene at 50°C

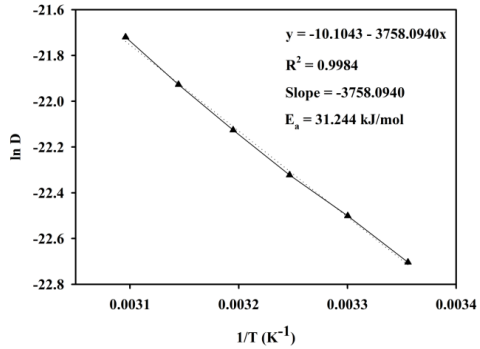

(g) Arrhenius plot of ln D versus $1/T$

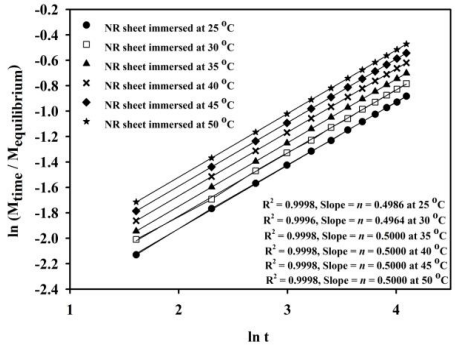

(h) Plots of ln ($M_{time}/M_{equilibrium}$) versus ln t

Fig. 10 Linear plots of fractional solvent uptake $M_{time}/M_{equilibrium}$ and $t^{1/2}$ for crosslinked NR sheets immersed in toluene

Fig. 10 illustrates the relationship between normalized solvent uptake ($M_{time}/M_{equilibrium}$ or M_t/M_∞ and $t^{1/2}$) for natural rubber sheets immersed in toluene at temperatures ranging from 25 to 50°C. A strong linear trend was observed during the initial swelling stage at all temperatures, indicating Fickian diffusion behavior. At 25°C (Fig. 10(a)), the slope was 0.0532, corresponding to a diffusion coefficient of 1.38×10^{-10} $m^2 \cdot s^{-1}$.

With increasing temperature, both the slope and diffusion coefficient increased progressively. At 30°C (Fig. 10(b)), 35°C (Fig. 10(c)), 40°C (Fig. 10(d)), 45°C (Fig. 10(e)), and 50°C (Fig. 10(f)), the slopes increased to 0.0588, 0.0642, 0.0696, 0.0751, and 0.0801, corresponding to diffusion coefficients of 1.69×10^{-10}, 2.20×10^{-10}, 2.46×10^{-10}, 3.00×10^{-10}, and 3.69×10^{-10} $m^2 \cdot s^{-1}$, respectively. This trend reflects enhanced solvent mobility due to increased chain mobility and transient free volume expansion at elevated temperatures [22, 30]. These results indicate that temperature plays a critical role in regulating solvent transport within the crosslinked rubber network.

Fig. 10(g) presents the Arrhenius plot for toluene diffusion through crosslinked natural rubber. The linear relationship across the full temperature range indicates thermally activated Arrhenius behavior. From the slope, the activation energy (E_a) of diffusion was calculated as 31.244 $kJ \cdot mol^{-1}$, suggesting a moderate energy barrier [30]. Fig. 10 (h) displays $\ln (M_{time}/M_{equilibrium})$ versus $\ln t$ plots for crosslinked natural rubber sheets immersed in toluene at 25-50°C. The diffusion exponent (n), determined from the slope, ranges from approximately 0.4964 to 0.5000, values characteristic of Fickian diffusion (n =0.5), where solvent transport follows concentration gradients and occurs much slower than polymer chain relaxation [22]. These findings suggest that toluene transport through crosslinked natural rubber follows Fickian behavior. The stable diffusion characteristics further support the structural integrity of the crosslinked network during solvent transport.

Tensile testing was conducted to evaluate the self-recovery capability of the crosslinked rubber network. The analysis assessed the extent to which the material restored its mechanical properties after mechanical loading. These results provide qualitative evidence of the material's recovery performance.

Fig. 11(a) presents the stress-strain behavior of the natural rubber sheets for the original uncut sample (0 min), and samples subjected to self-recovery for 60, 120, and 180 min after cutting. The original sample exhibited the highest stiffness and elastic modulus within the linear region, indicating a well-developed and intact crosslinked network. As the recovery time increased from 60 to 180 min, the stress–strain response gradually exhibited higher stiffness, accompanied by increases in elongation at break (%) and elastic modulus, as shown in Figs. 11(a)-11(c).

To quantitatively evaluate the recovery performance, the healing efficiency was calculated. The healing efficiency (%) shown in Fig. 11(d) was calculated using the following equation: healing efficiency (%) = (tensile strength after healing / tensile strength before healing) × 100%. The results indicate that increasing the self-recovery time has a positive effect on the healing efficiency (%), as longer healing durations lead to improved strength recovery, indicating that the crosslinked rubber network underwent time-dependent mechanical reconstruction. This behavior may be attributed to the formation of additional physical or ionic crosslinks [16].

Nevertheless, the self-recovered rubber exhibited lower mechanical performance than the original crosslinked material. Fig. 11(e) shows the crosslink density of the crosslinked natural rubber as a function of self-recovery time (60, 120, and 180 min), determined independently by the swelling method and rubber elasticity theory [28]. Both methods showed a gradual increase in crosslink density with increasing recovery time, supporting the progressive network reconstruction trend. These results provide complementary and consistent evidence of autonomous crosslink reformation across the rejoined interface at partially cut regions on the rubber surface (Fig.12).

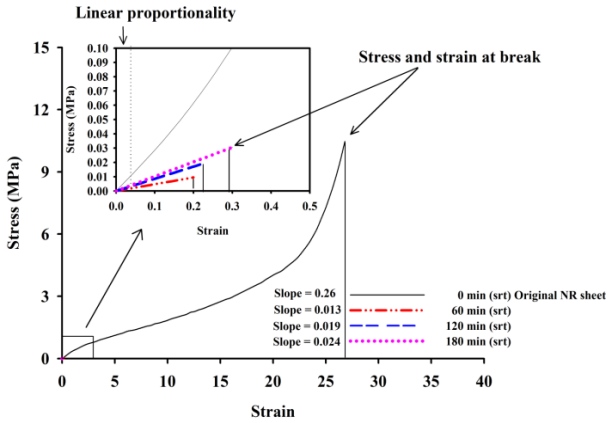

(a) Stress-strain curves

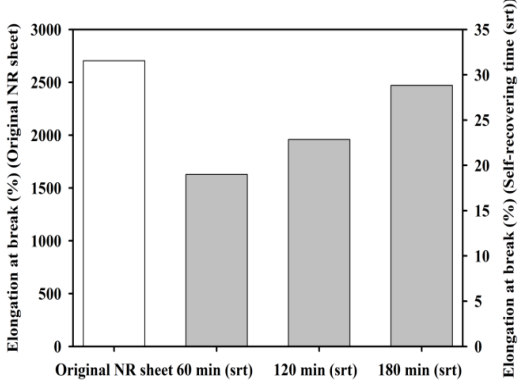

(b) Elongation at break (%)

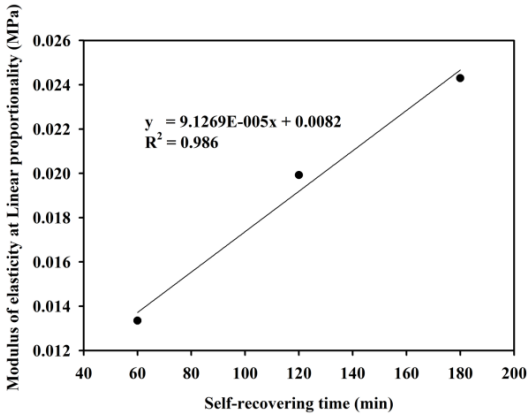

(c) Elastic modulus versus self-recovering time

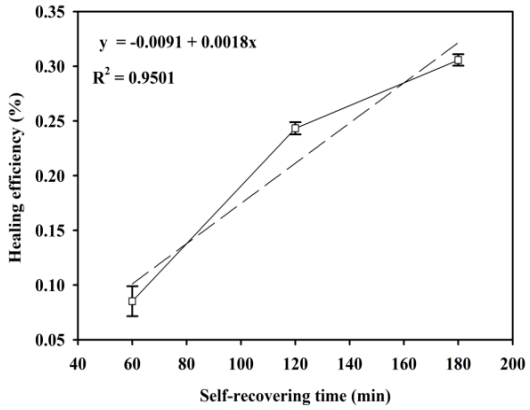

(d) Healing efficiency (%) versus self-recovering time

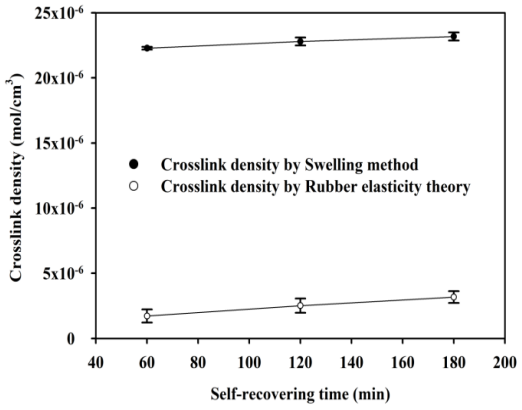

(e) Crosslink density versus self-recovering time

Fig. 11 Mechanical characterization and crosslink density of crosslinked natural rubber as a function of self-recovery time

3.3. Surface Morphology of Self-Recovering Crosslinked Natural Rubber as a Vascular Model

The surface morphology was initially examined in sheet form prior to fabrication into a tubular structure that replicates the geometry and functional characteristics of biological vascular tissue. Fig. 12 shows the surface morphology of the rubber sheet following controlled mechanical damage. Fig. 12(a) shows the undamaged rubber sheet, exhibiting a smooth and continuous surface without observable defects. In Fig. 12(b), a controlled cut was introduced to create a defined damage site. Figs. 12(c)-12(d) show the surface morphology at initiation and after 180 min of recovery, respectively. During the recovery process, the cut interface became progressively less defined, and surface continuity was gradually restored. Fig. 12(e) shows the surface after 180 min of recovery under tensile loading, demonstrating sufficient interfacial strength to withstand mechanical deformation and suggesting that the crosslinked rubber network underwent autonomous interfacial repair under ambient conditions.

(a) Undamaged rubber sheet

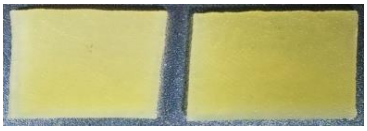

(b) Separated surfaces at the damaged interface

(c) Initial interfacial rejoining of rubber chains

(d) Recovered interface after 180 min of self-recovery

(e) Recovered interface after tensile loading at 180 min

Fig. 12 Optical images illustrating the self-recovery behavior of the crosslinked natural rubber sheet

3.4. Development and Performance Evaluation of a Wireless Electro-Syringe Injection System

The device operates on a closed-circuit detection principle. When the needle penetrates only into layer 1 without reaching layer 3, the circuit remains open, and both the LED and buzzer remain inactive, indicating a correct insertion depth within the vessel model (Fig. 13(a)). When the needle penetrates sufficiently to contact layer 3, the conductive needle bridges the two sensing layers, completing the circuit and simultaneously activating the LED and buzzer. This provides immediate visual and auditory feedback indicating excessive insertion depth (Fig. 13(b)). Experimental testing demonstrated rapid and reliable system response across repeated trials, consistent with sensor-integrated detection mechanisms increasingly used in medical training simulators for needle positioning and procedural feedback during simulated clinical interventions.

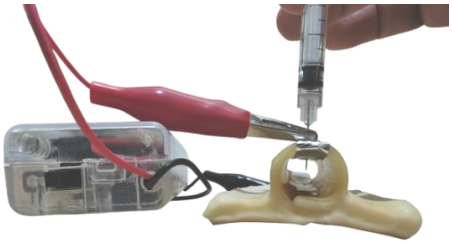

(a) Correct insertion depth

(b) Excessive needle penetration

Fig. 13 Operational states of the wireless electro-syringe injection during simulated needle insertion

Moreover, the integration of an autonomously self-recovering natural rubber vascular model with a wireless electronic sensing system produced a practical and low-cost device. In terms of operational durability, the material could be reused at least twice at the same position, as presented in Fig.12.

Compared with conventional silicone pad materials, the proposed crosslinked rubber demonstrated improved reusability due to its self-recovery capability, whereas commercial silicone materials generally lack self-healing behavior. In addition, most commercially available injection training devices remain manual and do not provide real-time feedback at an affordable cost. Although advanced intelligent systems have been reported, their high cost limits accessibility for medical students during skill training, which differs from the objectives of this study. The proposed system was cost-efficient, with an estimated cost of approximately 5-10 USD per unit, due to the use of simple, low-cost, and readily available electronic components.

In addition, the key findings were further clarified and strengthened through quantitative comparisons with previous studies [1-14]. The device performance, including penetration detection accuracy, response sensitivity, and real-time signal monitoring, was evaluated against existing systems reported in the literature [1-14]. The comparison suggests that the proposed

approach offers advantages in real-time detection capability and system responsiveness, thereby supporting the effectiveness of the developed device. Several limitations were also acknowledged, including the restricted evaluation under controlled experimental conditions and the absence of long-term testing. These factors may limit the generalizability and long-term applicability of the device in real clinical settings. However, these limitations could be addressed in future work through implementation in real learning environments to further assess the device's effectiveness as a training tool for improving medical students' clinical skills.

4. Conclusion

This study developed a wireless electro-syringe injection device for monitoring needle insertion depth during simulated injection procedures. The system integrated a closed-circuit electronic feedback mechanism with a self-recovering crosslinked natural rubber vascular sensor fabricated through controlled sulfur vulcanization of natural rubber latex. Material characterization indicated that higher vulcanization temperature and curing time increased crosslink density and reduced swelling, reflecting improved network formation. The material also exhibited time-dependent self-recovery, with mechanical properties and crosslink density recovering within 60-180 min under ambient conditions. Functional evaluation further demonstrated that the device reliably detected needle insertion depth, and the multilayer sensing system consistently distinguished correct placement from overpenetration through changes in electrical signals. The device demonstrated stable and repeatable performance. The main findings of this study are summarized as follows:

(1) The proposed device successfully achieved accurate real-time detection of needle penetration depth.
(2) The self-recovering natural rubber sensor exhibited effective structural recovery and reusability.
(3) The integration of a wireless electronic feedback system with a biomimetic sensor provided a practical and cost-effective platform for simulation-based injection training.

Overall, the findings demonstrated that integrating an autonomously self-recovering crosslinked natural rubber vascular model with a wireless sensing system enabled a practical, reusable, and economically accessible platform for injection training. Future work should focus on long-term implementation in real-world training environments to further evaluate the effectiveness of the system in improving medical students' injection skills.

Conflicts of Interest

The authors declare no conflict of interest.

References

[1] J. Micallef, A. Arutiunian, and A. Dubrowski, "The Development of an Intramuscular Injection Simulation for Nursing Students," Cureus, vol. 12, no. 12, article no. e12366, 2020.
[2] L. Lioce, S. Gunter, G. Maddux, I. Fogle, and B. Schroer, "Development of a Needle Injection Pad Trainer for Simulating Intradermal, Subcutaneous and Intramuscular Injections: Used in Student Nurse Training," Proceedings of the 33rd European Modeling and Simulation Symposium (EMSS 2021), pp. 253-259, 2021.
[3] B. R. Bhagat, M. Khairnar, P. P. Waknis, and B. M. Rudagi, "Innovative Pre-Clinical Learning in Oral Surgery: Injection on Tomato-AQuasi-Experimental Study," Journal of Maxillofacial and Oral Surgery, vol. 24, no. 1, pp. 8-12, 2025.
[4] A. M. Salameh Khraisat, H. Hapidin, N. S. H. Nik Ahmad, M. D. Mohammad Yusoff, M. S. Nurumal, and K. W. Pardi, "A Virtual Learning Environment for Teaching Intramuscular Injection: A Focus Group Discussion Analysis," Indian Journal of Forensic Medicine and Toxicology, vol. 14, no. 4, pp. 705-709, 2020.
[5] G. Avşar, Ş. Çelik, S. Doğan, and B. Çiftçi, "Virtual Reality Technology in Nursing Education: A Qualitative Study," European Journal of Education, vol. 59, no. 4, article no. e12780, 2024.
[6] K. Hanfati, S. Sukaridhoto, D. K. Basuki, R. P. N. Budiarti, E. D. Fajrianti, and I. A. Al Hafidz, "Design and Implementation of WebXR Health Learning Module Application," Proceedings of the 2022 International Electronics Symposium (IES), pp. 632-637, 2022.

[7] N. Soto-Ruiz, P. Escalada-Hernández, A. Bujanda-Sainz de Murieta, T. Ballesteros-Egüés, A. Larrayoz-Jiménez, y L. San Martín-Rodríguez, "Augmented Reality for Intramuscular Injection Training: A Cluster Randomized Controlled Trial," Teaching and Learning in Nursing, vol. 20, no. 3, pp. e869-e876, 2025.

[8] B. Terzi and A. Ilgaz, "The Effect of Flipped Classroom Model and Kahoot for Intramuscular Injection Training on Nursing Students' Knowledge, Skills and Self-Efficacy Levels," Journal of Nursology, vol. 27, no. 3, pp. 237-247, 2024.

[9] B. Terzi and S. Darıcı, "The Effect of Ventrogluteal Intramuscular Injection Training with Animated Video Containing Subliminal Messages: A Randomized Controlled Study," Journal of Nursing Effect, vol. 16, no. 3, pp. 304-316, 2023.

[10] Ö. Doğu and Ö. Tiryaki, "The Effect of the Interactive Workshop, E-Learning and Practice Training Given to Nurses on Injection to the Ventrogluteal Region on the Knowledge and Practices of Nurses," Karya Journal of Health Sciences, vol. 4, no. 1, pp. 60-64, 2023.

[11] E. Y. Coskun and M. Sendir, "Effectiveness of Computer-Based and Hybrid Simulation in Teaching Intramuscular Medication Administration," International Journal of Caring Sciences, vol. 15, no. 2, pp. 1565-1575, 2022.

[12] K. Fujimoto, T. Kanamoto, S. Otani, R. Miyazaki, K. Ebina, and K. Nakata, "Basic Research for Ultrasound-Guided Injection into Skeletal Muscle Lesions in an Experimental Animal Model," Bone and Joint Research, vol. 14, no. 1, pp. 33-41, 2025.

[13] A. J. S. McCartan and R. J. Mrsny, "In Vitro Modeling of Intramuscular Injection Site Events," Expert Opinion on Drug Delivery, vol. 21, no. 8, pp. 1155-1173, 2024.

[14] R. Uppuluri, A. Bhattacharjee, S. Anwar, and Y. She, "SeeBelow: Sub-Dermal 3D Reconstruction of Tumors with Surgical Robotic Palpation and Tactile Exploration," Proceedings of the IEEE/RSJ International Conference on Intelligent Robots and Systems (IROS), IEEE Press, pp. 6961-6968, 2024.

[15] ASTM D3616-95, Standard Test Method for Rubber-Determination of Gel, Swelling Index, and Dilute Solution Viscosity, ASTM International, 1995.

[16] C. Xu, L. Cao, B. Lin, X. Liang, and Y. Chen, "Design of Self-Healing Supramolecular Rubbers by Introducing Ionic Cross-Links into Natural Rubber via a Controlled Vulcanization," ACS Applied Materials and Interfaces, vol. 8, no. 27, pp. 17728-17737, 2016.

[17] C. Kumnuantip and N. Sombatsompop, "Dynamic Mechanical Properties and Swelling Behaviour of NR/Reclaimed Rubber Blends," Materials Letters, vol. 57, no. 21, pp. 3167-3174, 2003.

[18] P. J. Flory and J. Rehner, "Statistical Mechanics of Cross-Linked Polymer Networks II. Swelling," The Journal of Chemical Physics, vol. 11, no. 11, pp. 521-526, 1943.

[19] ASTM D471-16, Standard Test Method for Rubber Property-Effect of Liquids, ASTM International, 2016.

[20] J. Crank, The Mathematics of Diffusion, 2nd ed., Oxford, U.K.: Oxford University Press, 1975.

[21] W. D. Callister and D. G. Rethwisch, Materials Science and Engineering: An Introduction, 10th ed., Hoboken, NJ: Wiley, 2020.

[22] R. W. Korsmeyer, R. Gurny, E. Doelker, P. Buri, and N. A. Peppas, "Mechanisms of Solute Release from Porous Hydrophilic Polymers," International Journal of Pharmaceutics, vol. 15, no. 1, pp. 25-35, 1983.

[23] J. D. Ferry, Viscoelastic Properties of Polymers, 3rd ed., New York: Wiley, 1980.

[24] M. Akiba and A. S. Hashim, "Vulcanization and Crosslinking in Elastomers," Progress in Polymer Science, vol. 22, no. 3, pp. 475-521, 1997.

[25] S. Muroga, Y. Takahashi, Y. Hikima, S. Ata, M. Ohshima, T. Okazaki, et al., "New Evaluation Method for the Curing Degree of Rubber and Its Nanocomposites Using ATR-FTIR Spectroscopy," Polymer Testing, vol. 93, article no. 106993, 2021.

[26] ASTM D412-21, Standard Test Methods for Vulcanized Rubber and Thermoplastic Elastomers-Tension, ASTM International, 2021.

[27] D. Roylance, Stress-Strain Curves, Cambridge, MA: Massachusetts Institute of Technology, 2001.

[28] P. J. Flory, Statistical Mechanics of Chain Molecules, New York: Wiley, 1969.

[29] B. Stuart, Infrared Spectroscopy: Fundamentals and Applications, Chichester, UK: Wiley, 2004.

[30] A. Y. Coran, Vulcanization in Science and Technology of Rubber, 2nd ed., B. Erman and J. E. Mark, Eds. San Diego, CA, USA: Academic Press, pp. 339-385, 1994.